Estimating the Thermodynamic and Dynamic Contributions to Hydroclimatic Change over Peninsular Florida

VASUBANDHU MISRA[a,b,c] AND AMIT BHARDWAJ[b,c]

[a] *Department of Earth, Ocean and Atmospheric Science, Florida State University, Tallahassee, Florida*
[b] *Center for Ocean-Atmospheric Prediction Studies, Florida State University, Tallahassee, Florida*
[c] *Florida Climate Institute, Florida State University, Tallahassee, Florida*

(Manuscript received 28 June 2020, in final form 17 October 2020)

ABSTRACT: In this study we examine the thermodynamically and dynamically forced hydroclimatic changes in the four representative seasons over Peninsular Florida (PF) from an unprecedented pair of high-resolution regional coupled ocean–atmosphere model simulations conducted at 10-km grid spacing for both the atmospheric and the oceanic components forced by one of the global climate models that participated in CMIP5. The model simulation verifies reasonably well with the observations and captures the distinct seasonal cycle of the region. The projected change in the freshwater flux in the mid-twenty-first century (2041–60) relative to the late twentieth century (1986–2005) shows a precipitation deficit in the summer over PF, which is statistically significant. This projected change in freshwater flux over PF is enabled by the strengthening of the anticyclonic North Atlantic subtropical high circulation with corresponding changes in divergence of moisture, advection of moisture from changes in the winds and in the change in humidity gradient, and from the change in moisture flux convergence by the transient eddies. These changes suggest that a future warm climate could witness a drier summer over PF at the expense of a wetter West Florida Shelf. The analysis conducted in this study reveals that the changes in atmospheric circulation have a significant impact on the hydroclimate, far more than that implied by the Clausius–Clapeyron equation from changes in temperature.

KEYWORDS: North America; Atmosphere-land interaction; Atmosphere-ocean interaction; Hydrometeorology; Regional models; Seasonal variability

1. Introduction

Peninsular Florida (PF) sits on the border of the tropics and the extratropics, which makes for its unique geography in the continental United States. Thus, small shifts in the distinct circulation patterns and the thermodynamics of the tropics and extratropics tend to have a profound impact on PF (Selman et al. 2013; Kirtman et al. 2017). In addition, the robust ocean circulations around PF (Misra and Mishra 2016; Misra et al. 2017a) are known to affect the hydroclimate over PF. In fact, Misra et al. (2017a,b) show that the seasonal cycle of the hydroclimate over PF, the Loop and the Florida Currents, and the seasonal cycle of the upper-ocean temperatures in the West Florida Shelf and along the eastern coast of PF are all nearly in phase with each other. Misra and Mishra (2016) indicate that this overlap in the seasonal cycle of the upper ocean and that of the hydroclimate of PF are not a mere coincidence but are part of a complex feedback process. For example, the increased evaporation from the neighboring warming oceans in early summer increases the sub-cloud-layer entropy and eventually leads to a breakout of in situ convection at the expense of reduced precipitation over PF (Misra and Mishra 2016).

The resolution of the Loop Current and its eddies affect the ocean heat content in the neighboring ocean waters of PF (Liu et al. 2015; Misra et al. 2017b), which then affects the overlying atmosphere (Kirtman et al. 2012; Putrasahan et al. 2017) and precipitation variability over PF (Bhardwaj and Misra 2019). Misra et al. (2019) showed that downscaling of global climate model simulations over PF using a regionally coupled ocean–atmosphere model yielded a climate projection in the mid-twenty-first century over PF that was significantly different from the corresponding driving global model projection for PF. For example, the driving global model in Misra et al. (2019) indicated a projection of insignificant change in annual mean precipitation over PF, while the dynamically downscaled climate from this global model using a regional coupled ocean–atmosphere model suggested significant drying. This was attributed to the significant warming that occurred over the West Florida Shelf in the regional model, largely triggered by a substantial reduction in the low-level clouds that increased the net atmospheric flux into the shallow waters of the West Florida Shelf. Therefore, Misra et al. (2019) argue that horizontal resolutions of ~10 km are necessary to project climate for a region like Florida, where there is considerable coastline, complex ocean bathymetry, and associated ocean circulations that give rise to a very distinct seasonality to the region.

In this study we have conducted a detailed moisture budget from the same pair of coupled ocean–atmosphere regional climate model (RCM) integrations for the current climate simulation and the future climate projection used in Misra et al. (2019). The intent here is not to intercompare the global model and the RCM hydroclimate over PF but to diagnose the important forcing terms in the moisture budget

Corresponding author: Vasubandhu Misra, vmisra@fsu.edu

DOI: 10.1175/JHM-D-20-0159.1

TABLE 1. Outline of the RCM.

Model	References
Ocean model (Regional Ocean Model System)	
30 vertical sigma levels on horizontal staggered Arakawa-C grid	Haidvogel et al. (2000); Shchepetkin and McWilliams (2005)
Boundary layer formulation	*K*-profile (Large et al. 1994)
Mixing scheme	Mellor and Yamada (1982); Umlauf and Burchard (2003)
Atmospheric model (Regional Spectral Model)	
28 vertical terrain following sigma levels with double sine-cosine series with wall boundary conditions as basis functions for horizontal discretization	Juang and Kanamitsu (1994)
Boundary layer	Hong and Pan (1996)
Clouds	Zhao and Carr (1997)
Deep convection	Moorthi and Suarez (1992)
Gravity wave drag	Alpert et al. (1988)
Land model	Ek et al. (2003)
Longwave radiation	Chou and Lee (1996)
Shallow convection	Tiedtke (1983)
Shortwave radiation	Chou and Suarez (1994)

of the projections from the RCM. Further details of the RCM and the integrations analyzed in this paper are provided in the following section.

2. Model description and experiment design

The RCM used in this study has been extensively used for regional climate studies across the world (Li et al. 2012, 2014; Ham et al. 2016; Misra et al. 2018) and in particular over Florida (Misra and Mishra 2016; Misra et al. 2019). The RCM is unique in using identical grids for both ocean and atmosphere components of the model and avoids using any flux coupler or any flux corrections. The atmospheric component is the regional spectral model following Juang and Kanamitsu (1994), which has gone through several rounds of modification detailed in subsequent publications (e.g., Misra et al. 2019). The ocean component of the RCM is regional ocean model system following Shchepetkin and McWilliams (2005). A brief outline of the two components of the RCM is provided in Table 1.

These RCM integrations were conducted at 10-km grid spacing for both the ocean and the atmospheric components of the model, over two 20-yr periods, representing the current climate (1986–2005, late twentieth century) and the future climate (2041–60, mid-twenty-first century) under representative concentration pathway (RCP) 8.5 emission scenario. These integrations were forced with Community Climate System Model version 4 (CCSM4; Gent et al. 2011), which was part of the Coupled Model Intercomparison Project phase 5 (CMIP5; Taylor et al. 2012).

For verification of the late-twentieth-century simulation, we make use of the daily rainfall data from the Integrated Multisatellite Retrievals for Global Precipitation Mission version 6 (IMERG; Huffman et al. 2019). These rainfall data are available globally at 0.1° grid spacing from 1 June 2000 to the present. Although this dataset does not overlap with our late-twentieth-century (1986–2005) RCM simulation, it still provides us a robust 20-yr climatology covering both land and the oceans at a resolution that is comparable to the RCM. We also make use of the Climate Prediction Center global daily temperature available at 0.5° grid spacing from 1981 to 2010 from https://psl.noaa.gov/ for verifying land surface temperature from the RCM simulation. To verify the total precipitable water in the RCM simulation we made use of corresponding total precipitable water from the NASA Water Vapor Project (NVAP; https://eosweb.larc.nasa.gov/sites/default/files/project/nvap/readme/ASDC_NVAP_Overview_2016.pdf; doi:10.5067/NVAP-M/NVAP_CLIMATE_Total-Precipitable-Water_L3.001). This dataset is available globally from 1988 to 2009 at 1° grid spacing.

3. Methodology

The vertically integrated moisture budget equation, following Trenberth and Guillemot (1995) and Zhao and Carr (1997) can be written as

$$R - E = R_C + R_L - E = -\frac{\partial Q}{\partial t} - \frac{\partial Q_c}{\partial t} - \frac{q_{\text{surf}}}{g}\frac{\partial p_{\text{surf}}}{\partial t} - \frac{qc_{\text{surf}}}{g}\frac{\partial p_{\text{surf}}}{\partial t} - \frac{1}{g}\int_{p_{\text{top}}}^{p_{\text{surf}}} \nabla \cdot \mathbf{V} q \, dp - \frac{1}{g}\int_{p_{\text{top}}}^{p_{\text{surf}}} \nabla \cdot \mathbf{V} qc \, dp, \tag{1}$$

where R is precipitation, R_C is the convective precipitation handled by the relaxed Arakawa–Schubert scheme (Moorthi and Suarez 1992), R_L is the large-scale precipitation handled by the Zhao and Carr scheme (1997) in the regional spectral model, E is surface evaporation, $Q = (1/g)\int_{p_{\text{top}}}^{p_{\text{surf}}} q \, dp$, $Q_c = (1/g)\int_{p_{\text{top}}}^{p_{\text{surf}}} qc \, dp$, p_{top} and p_{surf} are pressure at the top and at the surface of the atmospheric column, q is specific humidity, qc is the cloud water mixing ratio, q_{surf} is surface specific humidity, qc_{surf} is surface cloud water mixing ratio, and $\mathbf{V}$ is the horizontal wind vector. Now, if the variables in Eq. (1) are divided into time-mean (denoted by overbar) and transient (denoted by prime) components, then Eq. (1) can be written as

$$\overline{R}-\overline{E}=-\frac{\partial\overline{Q}}{\partial t}-\frac{\partial\overline{Q}_c}{\partial t}-\frac{\overline{q}_{\text{surf}}}{g}\left(\frac{\partial\overline{p}_{\text{surf}}}{\partial t}\right)-\frac{\overline{qc}_{\text{surf}}}{g}\left(\frac{\partial\overline{p}_{\text{surf}}}{\partial t}\right)\underbrace{-\frac{1}{g}\int_{p_{\text{top}}}^{p_{\text{surf}}}\nabla\cdot(\overline{\mathbf{V}}\,\overline{q})\,dp}_{\text{Term A}_1}$$
$$\underbrace{-\frac{1}{g}\int_{p_{\text{top}}}^{p_{\text{surf}}}\nabla\cdot(\overline{\mathbf{V}}\,\overline{qc})\,dp}_{\text{Term B}_1}\ \underbrace{-\frac{1}{g}\int_{p_{\text{top}}}^{p_{\text{surf}}}\nabla\cdot(\overline{\mathbf{V}'q'})\,dp}_{\text{Term A}_2}\ \underbrace{-\frac{1}{g}\int_{p_{\text{top}}}^{p_{\text{surf}}}\nabla\cdot(\overline{\mathbf{V}'qc'})\,dp}_{\text{Term B}_2}$$
$$-q_{\text{surf}}\mathbf{V}_{\text{surf}}\cdot\nabla p_{\text{surf}}-qc_{\text{surf}}\mathbf{V}_{\text{surf}}\cdot\nabla p_{\text{surf}}, \tag{2}$$

where the overbar represents the monthly mean and the prime denotes the departure from the monthly mean (or submonthly transients), terms A_1 and B_1 are water vapor and cloud water flux divergence contributed by the monthly mean, and terms A_2 and B_2 are the water vapor and cloud water flux divergence contributed by the submonthly transients, respectively. The last two terms on the right-hand side of Eq. (2) have not been decomposed into time-mean and transient components. In this study, we use January, April, July, and October as representative months for winter, spring, summer, and fall seasons. Some of the terms in Eq. (2) can be further decomposed to divergence and advection components as

$$\overbrace{\overline{R}-\overline{E}}^{\text{Term 1}}=\overbrace{-\frac{\partial\overline{Q}}{\partial t}}^{\text{Term 2}}\overbrace{-\frac{\partial\overline{Q}_c}{\partial t}}^{\text{Term3}}\overbrace{-\frac{1}{g}\int_{p_{\text{top}}}^{p_{\text{surf}}}\overline{q}\nabla\cdot\overline{\mathbf{V}}\,dp}^{\text{Term 4}}\overbrace{-\frac{1}{g}\int_{p_{\text{top}}}^{p_{\text{surf}}}\overline{\mathbf{V}}\cdot\nabla\overline{q}\,dp}^{\text{Term 5}}\overbrace{-\frac{1}{g}\int_{p_{\text{top}}}^{p_{\text{surf}}}\nabla\cdot(\overline{\mathbf{V}'q'})\,dp}^{\text{Term 6}}$$
$$\overbrace{-\frac{1}{g}\int_{p_{\text{top}}}^{p_{\text{surf}}}\overline{qc}\nabla\cdot\overline{\mathbf{V}}\,dp}^{\text{Term 7}}\overbrace{-\frac{1}{g}\int_{p_{\text{top}}}^{p_{\text{surf}}}\overline{\mathbf{V}}\cdot\nabla\overline{qc}\,dp}^{\text{Term 8}}\overbrace{-\frac{1}{g}\int_{p_{\text{top}}}^{p_{\text{surf}}}\nabla\cdot(\overline{\mathbf{V}'qc'})\,dp}^{\text{Term 9}}$$
$$\underbrace{-\frac{1}{g}(\overline{q}_{\text{surf}}\overline{\mathbf{V}}_{\text{surf}}+\overline{q'_{\text{surf}}\mathbf{V}'_{\text{surf}}}+\overline{qc}_{\text{surf}}\overline{\mathbf{V}}_{\text{surf}}+\overline{qc'_{\text{surf}}\mathbf{V}'_{\text{surf}}})\cdot\nabla\overline{p}_{\text{surf}}-\frac{\overline{q}_{\text{surf}}}{g}\left(\frac{\partial\overline{p}_{\text{surf}}}{\partial t}\right)-\frac{\overline{qc}_{\text{surf}}}{g}\left(\frac{\partial\overline{p}_{\text{surf}}}{\partial t}\right)}_{\text{Term Res}}. \tag{3}$$

In the above equation, we compute each of the terms from the RCM output (available daily at 10 pressure levels on a 10-km latitude/longitude grid) and term Res is obtained as a residue.

To evaluate the differences in the individual terms of Eq. (3) between the mid-twenty-first-century projection and the late-twentieth-century simulation of the RCM, we follow Seager et al. (2010) to denote

$$\delta(.)=(.)_{\text{M21st}}-(.)_{\text{L20th}}, \tag{4}$$

where subscripts M21st and L20th indicate the values of the various terms of Eq. (3) evaluated from the mid-twenty-first-century (2041–60) and the late-twentieth-century (1986–2005) climate simulations, respectively. Therefore, operating Eq. (4) on Eq. (3) [viz., substituting the right-hand side of Eq. (3) in to $()_{\text{M21st}}$ for the mid-twenty-first-century simulations and $()_{\text{L20th}}$ for the late-twentieth-century simulations] yields:

$$\overbrace{\delta(\overline{R}-\overline{E})}^{\text{Term A}}=\overbrace{-\frac{\partial\delta\overline{Q}}{\partial t}}^{\text{Term B}}\overbrace{-\frac{\partial\delta\overline{Q}_c}{\partial t}}^{\text{Term C}}\overbrace{-\frac{1}{g}\int_{p_{\text{top}}}^{p_{\text{surf}}}\delta\overline{q}\nabla\cdot\overline{\mathbf{V}}_{\text{L20th}}\,dp}^{\text{Term D}}\overbrace{-\frac{1}{g}\int_{p_{\text{top}}}^{p_{\text{surf}}}\overline{q}_{\text{L20th}}\nabla\cdot\delta\overline{\mathbf{V}}}^{\text{Term E}}\overbrace{-\frac{1}{g}\int_{p_{\text{top}}}^{p_{\text{surf}}}\overline{\mathbf{V}}_{\text{L20th}}\cdot\nabla\delta\overline{q}}^{\text{Term F}}$$
$$\overbrace{-\frac{1}{g}\int_{p_{\text{top}}}^{p_{\text{surf}}}\delta\overline{qc}\nabla\cdot\overline{\mathbf{V}}_{\text{L20th}}\,dp}^{\text{Term G}}\overbrace{-\frac{1}{g}\int_{p_{\text{top}}}^{p_{\text{surf}}}\overline{qc}_{\text{L20th}}\nabla\cdot\delta\overline{\mathbf{V}}}^{\text{Term H}}\overbrace{-\frac{1}{g}\int_{p_{\text{top}}}^{p_{\text{surf}}}\overline{\mathbf{V}}_{\text{L20th}}\cdot\nabla\delta\overline{qc}}^{\text{Term I}}$$
$$\overbrace{-\frac{1}{g}\int_{p_{\text{top}}}^{p_{\text{top}}}\delta\overline{\mathbf{V}}\cdot\nabla\overline{q}_{\text{L20th}}}^{\text{Term J}}\overbrace{-\frac{1}{g}\int_{p_{\text{top}}}^{p_{\text{surf}}}\nabla\cdot\delta(\overline{\mathbf{V}'q'})\,dp}^{\text{Term K}}\overbrace{-\frac{1}{g}\int_{p_{\text{top}}}^{p_{\text{surf}}}\nabla\cdot(\delta\overline{\mathbf{V}}\delta\overline{q})\,dp}^{\text{Term L}}$$
$$\overbrace{-\frac{1}{g}\int_{p_{\text{top}}}^{p_{\text{top}}}\delta\overline{\mathbf{V}}\cdot\nabla\overline{qc}_{\text{L20th}}}^{\text{Term M}}\overbrace{-\frac{1}{g}\int_{p_{\text{top}}}^{p_{\text{surf}}}\nabla\cdot\delta(\overline{\mathbf{V}'qc'})\,dp}^{\text{Term N}}\overbrace{-\frac{1}{g}\int_{p_{\text{top}}}^{p_{\text{surf}}}\nabla\cdot(\delta\overline{\mathbf{V}'}\delta\overline{qc})\,dp}^{\text{Term O}}\overbrace{-\delta\text{Res}}^{\text{Term P}}. \tag{5}$$

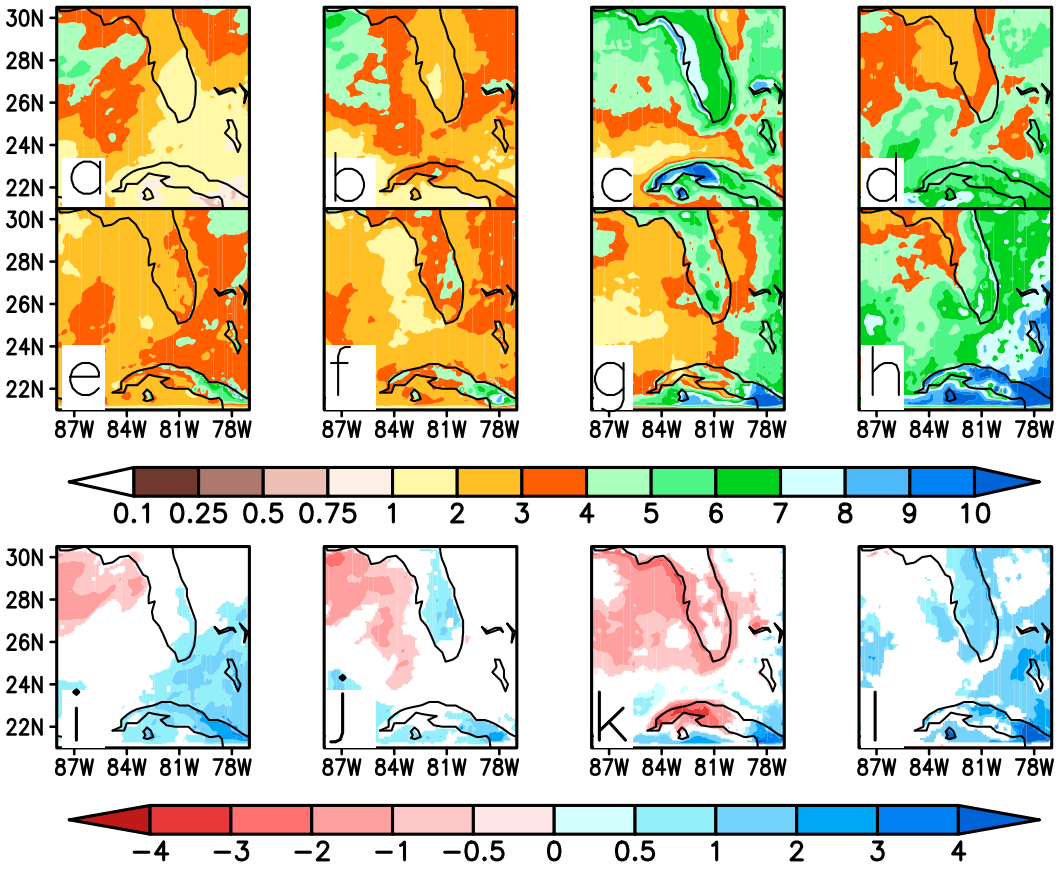

FIG. 1. The (top) observed IMERG, (middle) RCM simulated climatology of rainfall, and (bottom) their corresponding differences (RCM simulation − observations) for (a),(e),(i) January; (b),(f),(j) April; (c),(g),(k) July; and (d),(h),(l) October (all units are mm day^{-1}). The differences in (i)–(l) are shaded if they exceed 95% confidence interval according to a *t* test.

In Eq. (5), terms involving changes in $\overline{q}$and $\overline{qc}$ but not $\overline{\mathbf{V}}$ are referred to as thermodynamic contributors to $(\overline{R}-\overline{E})$. From Eq. (5) these thermodynamic contributors are terms B, C, D, F, G, and I. Furthermore, we resolve some of these terms into contributions due to divergence of water vapor (terms D and G) and advection of water vapor (terms F and I). Similarly, terms involving changes in $\overline{\mathbf{V}}$ but not in $\overline{q}$ and $\overline{qc}$ in Eq. (5) are called as dynamic contributors (terms E, H, J, and M). They can be further classified as those due to divergence (terms E and H) and those due to advection (terms J and M). The transient terms like terms K, L, N, and O involve covariance, and it is difficult to separate them as contributions from eddy flow and eddy scalar (≡ humidity/cloud water mixing ratio). Term P relates to changes in surface pressure and some other surface scalar variables. In Eq. (5), all of the terms are computed separately from the RCM output with terms L + O + P, which is computed as a residue.

4. Results

a. Model validation

In Figs. 1a–d we show the observed climatological seasonal cycle of precipitation over the domain of the RCM. The seasonal cycle is most apparent over PF where January (Fig. 1a) and April (Fig. 1b) represent the drier part of the year while July (Fig. 1c) represents the wettest part of the year followed by that in October (Fig. 1d). The neighboring oceans, especially the West Florida Shelf also show a similar seasonal cycle as PF, albeit with a smaller amplitude (Fig. 1). The corresponding RCM climatology in Figs. 1e–h show that in broad terms this seasonal cycle over PF and its contrast with a milder seasonal cycle of precipitation in the neighboring oceans is reasonably well simulated. The corresponding climatological errors of the RCM show that the month of January (Fig. 1i) has the least error overall while the month of October shows the most error over PF (Fig. 1l) and in July the errors are largest over the West Florida Shelf (Fig. 1k). Although the desire is always to minimize the climatological errors, the magnitude of the climatological errors in display from the RCM in Figs. 1i–l is very encouraging given that the RCM is a coupled ocean–atmosphere model, where feedbacks from upper-ocean errors can compound the model precipitation bias. The comparatively reduced climatological errors over PF in January (Fig. 1i) and in July (Fig. 1k) is helpful to contrast the hydroclimate budget from the RCM during the dry and wet parts of the year.

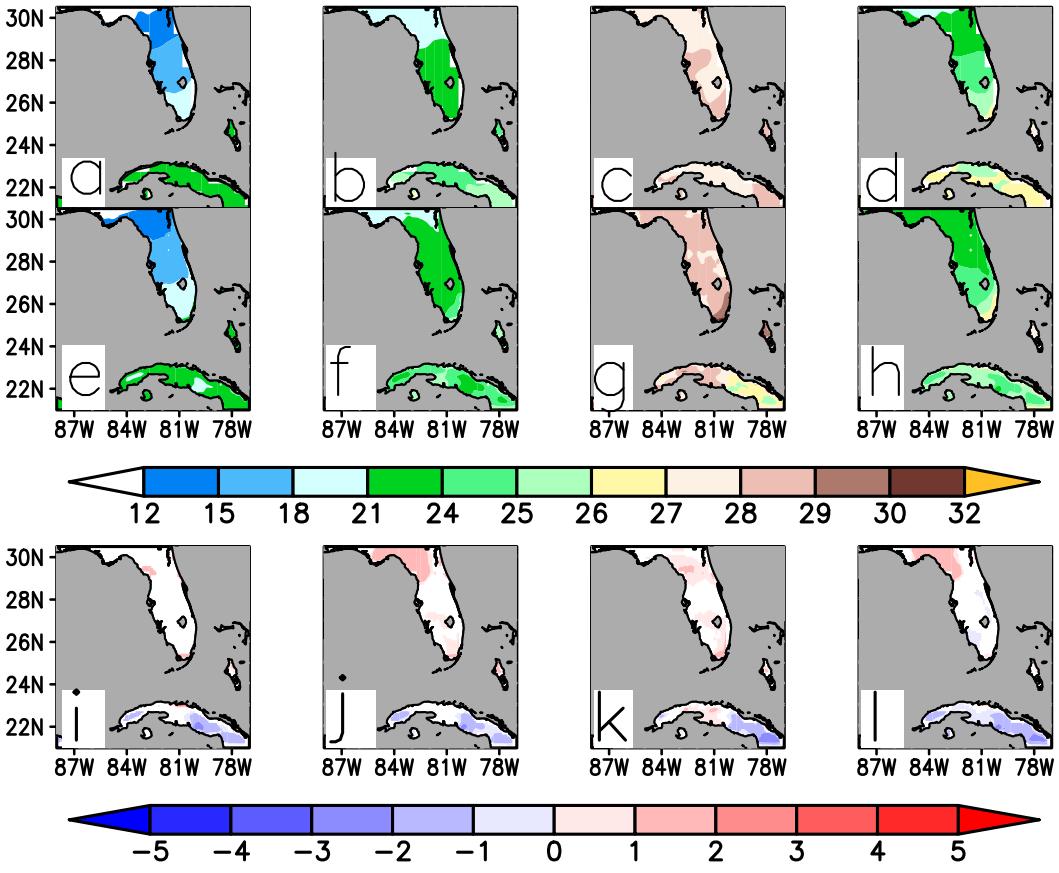

FIG. 2. The (top) observed CPC, (middle) RCM simulated climatology of land surface temperature, and (bottom) their corresponding differences (RCM simulation − observations) for (a),(e),(i) January; (b),(f),(j) April; (c),(g),(k) July; and (d),(h),(l) October (all units are °C). The differences in (i)–(l) are shaded if they exceed 95% confidence interval according to a *t* test.

In Fig. 2 we verify the climatological land surface temperature from the RCM simulation. Many studies have shown the relationship between surface temperature and rainfall (Trenberth et al. 2003; Held and Soden 2006; Utsumi et al. 2011; Westra et al. 2014). These studies have shown that mean rainfall and the annual daily maximum rainfall scale with temperature as a consequence of the Clausius–Clapeyron equation. Again, the observed seasonal cycle of the land surface temperature is robust over PF (Figs. 2a–d), with the seasonal contrast between say January and July is 10°–15°C across PF with the contrast being higher in northern part of PF. Furthermore, the contrast in the land surface temperature from south to north PF in the winter (Fig. 2a) and its diminishment in the summer (Fig. 2d) is also a feature of the seasonal cycle of PF (Misra et al. 2017b). These features of the seasonal cycle of the land surface temperature are well represented in the RCM simulation (Figs. 2e–h). It is quite apparent from Figs. 2i–l that the RCM simulation displays a high fidelity, especially in January (Fig. 2i). There is a slight warm bias in the northern part of PF that appears in April (Fig. 2j), July (Fig. 2k), and October (Fig. 2l).

The climatological seasonal cycle of the total precipitable water from the RCM simulation is verified in Fig. 3. The precipitable water or column integrated water vapor is also found to have an important relationship with temperature that scales with the Clausius–Clapeyron equation (Trenberth et al. 2003; Held and Soden 2006). Furthermore, Kunkel et al. (2013) find that probable maximum precipitation at a location has a strong linkage to water vapor. Trenberth et al. (2003) suggest that because of the increased moisture holding capacity of a warm atmosphere and ability of weather systems to gather moisture over extensive regions, it leads to increased convergence of moisture and more intense precipitation in a warming climate. Here, the lower precipitable water in the column over both PF and over the surrounding ocean is apparent in the observations during winter (Fig. 3a) and spring (Fig. 3b) relative to its peak in summer (Fig. 3c) and in fall (Fig. 3d). This observed seasonal cycle of the precipitable water is well replicated in the RCM simulation (Figs. 3e–h). But the largest dry bias in the precipitable water appears in the summer (Fig. 3k).

b. Projected change in precipitation

The seasonal cycle of precipitation in the mid-twenty-first century (Figs. 4a–d) is at least qualitatively similar to the late-twenty-first-century simulation (Figs. 1a–d) from the RCM. The climatologically drier months of January (Fig. 4a) and April

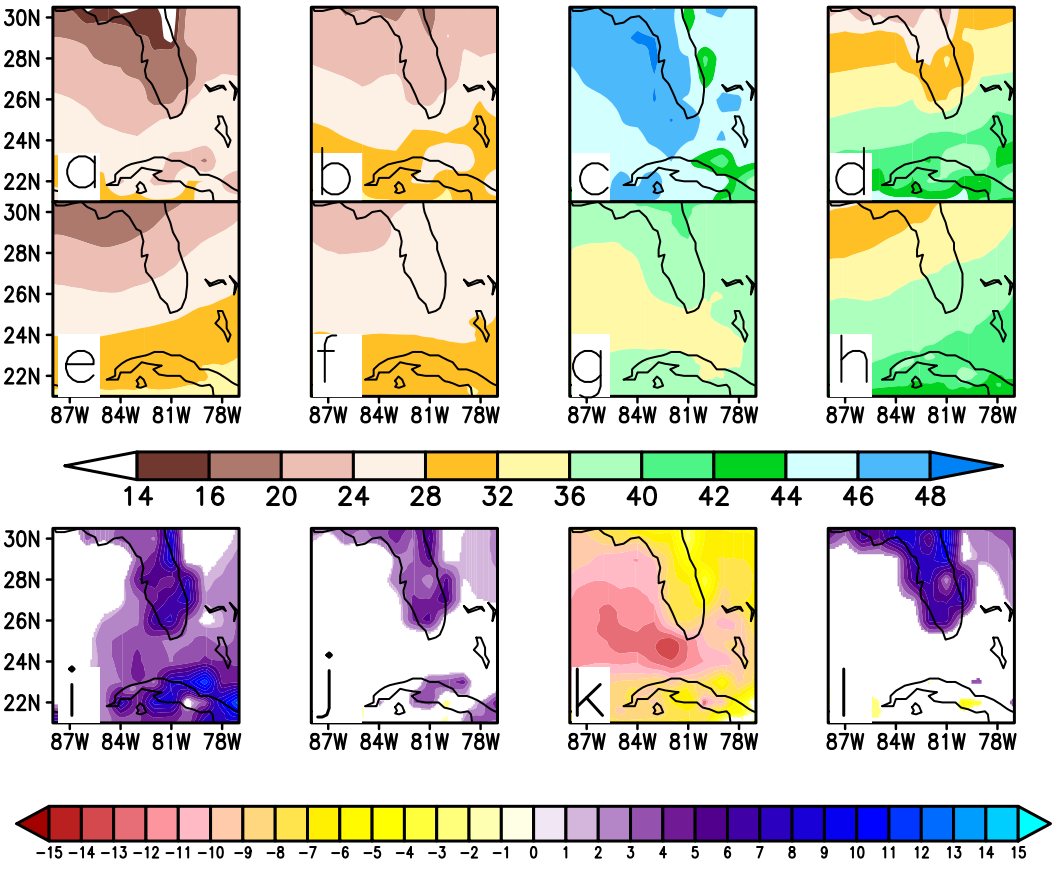

FIG. 3. The (top) observed NVAP, (middle) RCM simulated climatology of precipitable water, and (bottom) their corresponding differences (RCM simulation − observations) for (a),(e),(i) January; (b),(f),(j) April; (c),(g),(k) July; and (d),(h),(l) October (all units are kg m^{-2}). The differences in (i)–(l) are shaded if they exceed 95% confidence interval according to a t test.

(Fig. 4b) contrasts with the wetter months of July (Fig. 4c) and October (Fig. 4d), which is similar to the seasonal evolution of rainfall in the late-twentieth-century simulation (Figs. 1e–h). The RCM uniformly projects a reduction of rainfall in the future climate in all four seasons relative to the current climate over PF (Figs. 4e–h). However, the differences are largest and statistically significant only in July (summer; Fig. 4g). The contrast in the projected change in precipitation between the neighboring oceans and PF is also apparent in July (Fig. 4g). As Misra et al. (2019) indicate, these projected changes in rainfall from the RCM are different from the driving CCSM4 projections and also from the Fourth National Climate Assessment, which was based on the CMIP5 suite of models (USGCRP 2018). The interest in this paper, however, is not to compare and contrast the RCM and CCSM4 integrations, but to understand the projected hydroclimate changes over PF from the RCM. Furthermore, this comparison would be somewhat futile given the coarse resolution of the CCSM4 integration, which distorts the representation of PF and the West Florida Shelf (Misra et al. 2019).

c. *Moisture budget of the late-twentieth-century simulation*

In Figs. 5 and 6 we plot all the terms of Eq. (3) from the late-twentieth-century simulation of the RCM. In Table 2, the area-averaged values of the terms of Eq. (3) over PF are presented. The seasonal cycle of the freshwater flux $\overline{R}-\overline{E}$ in Figs. 5a–d is slightly different from that of precipitation (Figs. 1a–d). For instance, the freshwater flux peaks in October over PF and in some parts of the ocean around it (Fig. 5d; Table 2) and reaches a minimum in April (Fig. 5b). This feature is unlike other pluvial regions (e.g., monsoons) where precipitation dominates the freshwater flux. Over PF, the annual peak of surface temperature in the summer in combination with the fact that summer precipitation over PF is dominated by diurnal variations (e.g., sea breeze thunderstorms; Bastola and Misra 2013; Misra et al. 2017b) that produce cloud cover over limited spatiotemporal scales in the day, result in evaporation dominating the freshwater flux. It may be noted that none of the forcing terms of the moisture budget exactly follow this seasonal cycle of the freshwater flux (Figs. 5e–b1 and 6a,d, and Table 2).

The dominant terms of the moisture budget of the late-twentieth-century RCM simulation are the tendency of moisture due to the divergence of moisture [Figs. 5e–h; Table 2; term $4=-(1/g)\int_{p_{\rm top}}^{p_{\rm surf}}\overline{q}\nabla\cdot\overline{\mathbf{V}}\,dp$ of Eq. (3)], advection of moisture [Figs. 5i–l; Table 2; term $5=-(1/g)\int_{p_{\rm top}}^{p_{\rm surf}}\overline{\mathbf{V}}\cdot\nabla\overline{q}\,dp$ of

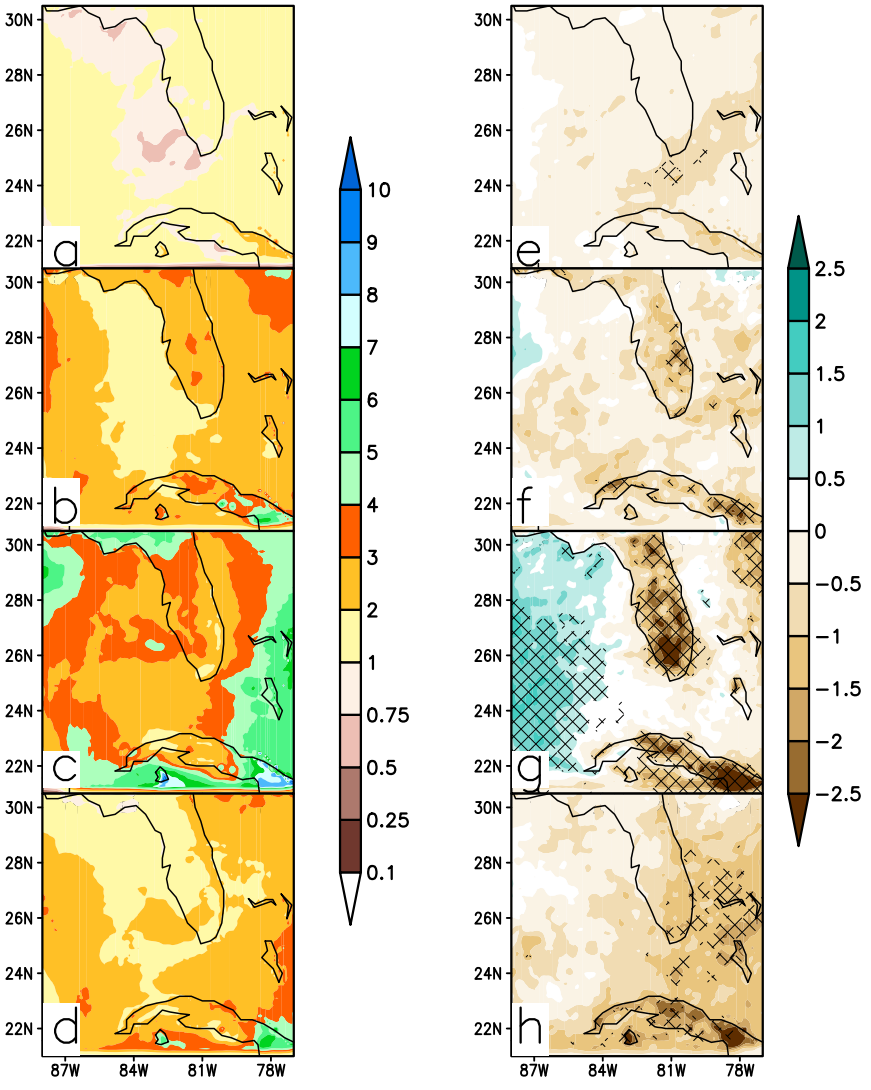

FIG. 4. The projected mean precipitation (mm day^{-1}) for mid-twenty-first century (2041–60) from the RCM simulations for (a) January, (b) April, (c) July, and (d) October. Its corresponding difference (mm day^{-1}) from the current (1986–2005) climate simulation for (e) January, (f) April, (g) July, and (h) October. The differences in (e)–(h) are hatched if they exceed 95% confidence interval according to a *t* test.

Eq. (3)], and moisture flux convergence by transient eddies [Figs. 5m–p; Table 2; term $6 = -(1/g)\int_{p_{top}}^{p_{surf}} \nabla \cdot (\overline{\mathbf{V}'q'})\, dp$ of Eq. (3)]. The corresponding terms of the moisture budget equation that involve the cloud water mixing ratio [e.g., term $7 = -(1/g)\int_{p_{top}}^{p_{surf}} \overline{qc}\nabla \cdot \overline{\mathbf{V}}\, dp \times 100$; term $8 = -(1/g)\int_{p_{top}}^{p_{surf}} \overline{\mathbf{V}} \cdot \nabla \overline{qc}\, dp \times 10$; term $9 = -(1/g)\int_{p_{top}}^{p_{surf}} \nabla \cdot (\overline{\mathbf{V}'qc'})\, dp$ of Eq. (3)] are far smaller (Figs. 5q–b1; Table 2). The residual term [Figs. 6a–d; Table 2; Term Res $= -(1/g)(\overline{q}_{surf}\overline{\mathbf{V}}_{surf} + \overline{q'_{surf}\mathbf{V}'_{surf}} + \overline{qc}_{surf}\overline{\mathbf{V}}_{surf} + \overline{qc'_{surf}\mathbf{V}'_{surf}}) \cdot \nabla\overline{p}_{surf} - (\overline{q}_{surf}/g)(\partial\overline{p}_{surf}/\partial t) - (\overline{qc}_{surf}/g)(\partial\overline{p}_{surf}/\partial t) + \epsilon$ of Eq. (3)] is small but are of the same order of magnitude as the dominant forcing terms (terms 4, 5, and 6). Note that we have added ε, which refers to contributions from numerical errors. It may be noted that the Res term is computed as a residue from Eq. (3). As Seager et al. (2010) note, that since the Res term is computed as a residue term from the diagnostic budget Eq. (3), the errors from the spatial and temporal discretization schemes also get implicitly added to this term. These errors arise because we are dealing with model output and are not conducting these budget calculations at every time step of the RCM integration on its native spatial grid.

The divergence of moisture displays a distinct seasonal cycle with maximum over PF in July and minimum over the surrounding oceans (Figs. 5e–h; Table 2). This is not surprising given that the divergent circulations from strong thunderstorm activities form over PF in the summer as noted in the observational study of Bastola and Misra (2013). In contrast, the advection of moisture shows a negative tendency over PF in July

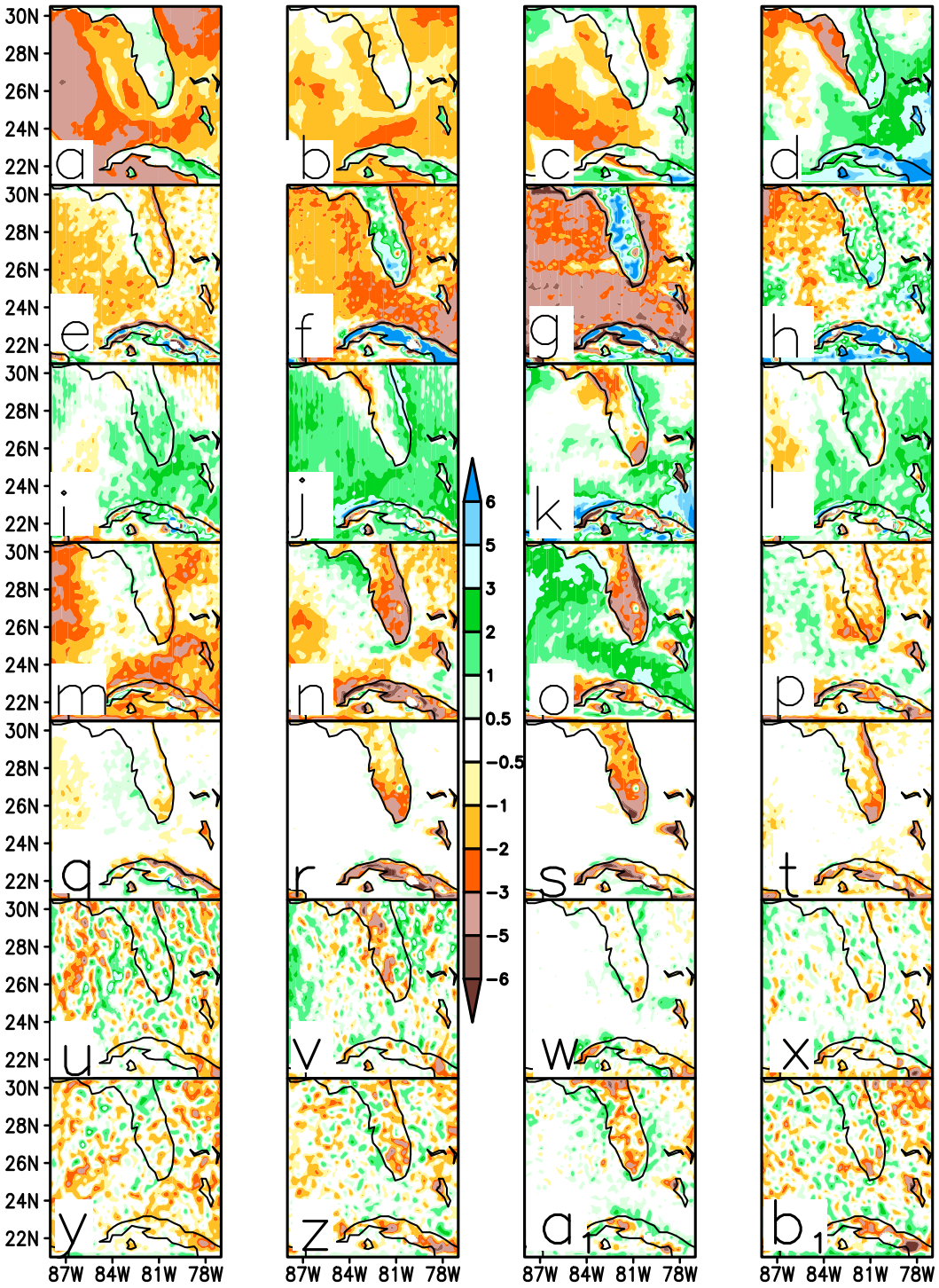

FIG. 5. The terms of the moisture budget (mm day^{-1}) from Eq. (3) for the current climate (1986–2005) RCM simulation showing (a)–(d) $\overline{R} - \overline{E}$, (e)–(h) term 4 [$= (1/g)\int_{p_{top}}^{p_{surf}} \overline{q}\nabla \cdot \overline{\mathbf{V}}\, dp$], (i)–(l) term 5 [$= -(1/g)\int_{p_{top}}^{p_{surf}} \overline{\mathbf{V}} \cdot \nabla\overline{q}\, dp$], (m)–(p) term 6 [$= -(1/g)\int_{p_{top}}^{p_{surf}} \nabla \cdot (\overline{\mathbf{V}'q'})\, dp$], (q)–(t) term 7 × 100 [$= -(1/g)\int_{p_{top}}^{p_{surf}} \overline{qc}\nabla \cdot \overline{\mathbf{V}}\, dp \times 100$], (u)–(x) term 8 × 10 [$= -(1/g)\int_{p_{top}}^{p_{surf}} \overline{\mathbf{V}} \cdot \nabla\overline{qc}\, dp \times 10$], and (y)–(b$_1$) term 9 × 10 [$= -(1/g)\int_{p_{top}}^{p_{surf}} \nabla \cdot (\overline{\mathbf{V}'qc'})\, dp \times 10$] for (left) January; (center left) April; (center right) July; and (right) October.

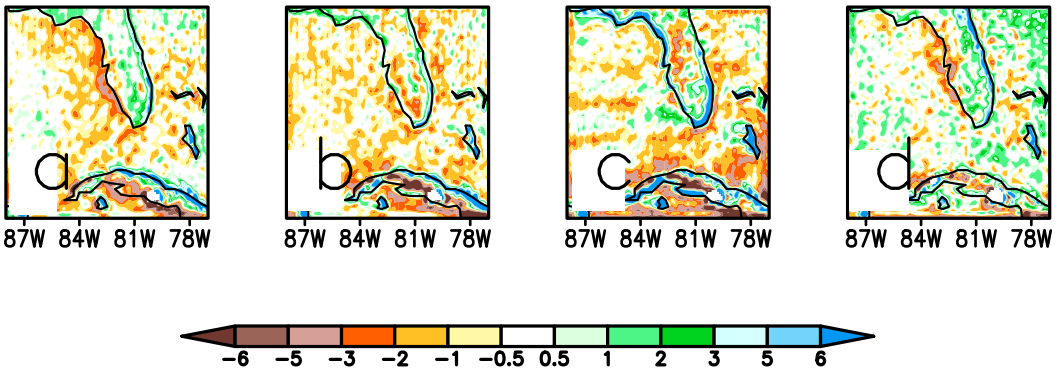

FIG. 6. The residual term Res [$= -(1/g)(\overline{q}_{\text{surf}}\overline{\mathbf{V}}_{\text{surf}} + \overline{q'_{\text{surf}}\mathbf{V}'_{\text{surf}}} + \overline{q}\overline{c}_{\text{surf}}\overline{\mathbf{V}}_{\text{surf}} + \overline{qc'_{\text{surf}}\mathbf{V}'_{\text{surf}}}) \cdot \nabla\overline{p}_{\text{surf}} - (\overline{q}_{\text{surf}}/g)\,(\partial\overline{p}_{\text{surf}}/\partial t) - (\overline{qc}_{\text{surf}}/g)(\partial\overline{p}_{\text{surf}}/\partial t)$; mm day^{-1}] of the moisture budget from Eq. (3) from the current climate (1986–2005) of the RCM simulation for (a) January, (b) April, (c) July, and (d) October.

(Fig. 5k; Table 2) with the strongest positive tendency over PF in October (Fig. 5l; Table 2) and widespread positive tendency over the ocean in April (Fig. 5j). The moisture flux convergence due to transient eddies shows there is a peak moisture flux divergence or negative moisture tendency over PF (Table 2) and positive moisture tendency over the surrounding oceans in July (Fig. 5o). The moisture tendency contribution from transient eddies at least over PF and the West Florida Shelf is a minimum in January (Fig. 5m; Table 2). The Res term also reaches a seasonal peak with positive moisture tendency over PF and the surrounding oceans in July (Fig. 6c; Table 2). But unlike terms 4, 5, and 6 of Eq. (3), it is not as spatially coherent.

d. *Projected change in the forcing of the hydroclimate change over PF*

Since it was shown that the projected change in precipitation was statistically significant only in July (Fig. 4), we focus only on this month for analyzing the projected hydroclimatic change. The area averaged values of the terms of Eq. (5) over PF is shown in Table 3. The projected change in the freshwater flux $\delta(\overline{R} - \overline{E})$ shows there is a negative and a positive change of the freshwater flux over PF (Table 3) and the surrounding oceans (Fig. 7a), respectively. The thermodynamic change due to divergence [term D $= -(1/g)\int_{p_{\text{top}}}^{p_{\text{surf}}} \delta\overline{q}\nabla \cdot \overline{\mathbf{V}}_{\text{L20th}}\, dp$ of Eq. (5)] is comparatively small (Fig. 7b; Table 3).

The dynamic change due to divergence [term E $= -(1/g)\int_{p_{\text{top}}}^{p_{\text{surf}}} \overline{q}_{\text{L20th}}\nabla \cdot \delta\overline{\mathbf{V}}\, dp$ of Eq. (5); Fig. 7c] shows similar spatial characteristics as that of the projected change of the freshwater flux (Fig. 7a), with negative tendencies over PF (Table 3) and positive tendencies over the West Florida Shelf. However, the dynamic change due to divergence shows with much higher spatial heterogeneity than the freshwater flux term, which is characteristic of the change in the divergence field.

The thermodynamic change due to advection [term F $= -(1/g)\int_{p_{\text{top}}}^{p_{\text{surf}}} \overline{\mathbf{V}}_{\text{L20th}} \cdot \nabla\delta\overline{q}\, dp$; Fig. 8d] shows that is nearly opposite to the projected change of the freshwater flux over PF (Table 3). In this case, term F tends to be uniformly positive both over PF and over the surrounding oceans (Fig. 7d).

TABLE 2. The area average values of the terms of Eq. (3) (mm day^{-1}).

Variable	January	April	July	October
$(\overline{R} - \overline{E})$	0.70	−0.44	0.35	1.95
Term 4 $\left(= -\frac{1}{g}\int_{p_{\text{top}}}^{p_{\text{surf}}} \overline{q}\nabla \cdot \overline{\mathbf{V}}\, dp\right)$	−0.84	1.39	2.65	1.06
Term 5 $\left(= -\frac{1}{g}\int_{p_{\text{top}}}^{p_{\text{surf}}} \overline{\mathbf{V}} \cdot \nabla\overline{q}\, dp\right)$	0.89	0.63	−0.83	0.81
Term 6 $\left[= -\frac{1}{g}\int_{p_{\text{top}}}^{p_{\text{surf}}} \nabla \cdot (\overline{\mathbf{V}'q'})\, dp\right]$	−0.27	−2.51	−2.88	−1.1
Term 7 × 100 $\left(= -\frac{1}{g}\int_{p_{\text{top}}}^{p_{\text{surf}}} \overline{qc}\nabla \cdot \overline{\mathbf{V}}\, dp \times 100\right)$	−0.18	−1.52	−2.27	−1.31
Term 8 × 100 $\left(= -\frac{1}{g}\int_{p_{\text{top}}}^{p_{\text{surf}}} \overline{\mathbf{V}} \cdot \nabla\overline{qc}\, dp \times 10\right)$	0.21	−0.86	−0.14	−0.04
Term 9 × 10 $\left[= -\frac{1}{g}\int_{p_{\text{top}}}^{p_{\text{surf}}} \nabla \cdot (\overline{\mathbf{V}'qc'})\, dp \times 10\right]$	−0.07	−0.76	−0.99	−0.22
Term Res	0.91	0.23	1.55	1.21

TABLE 3. The area average values over PF for terms of Eq. (5) (mm day^{-1}) for July.

Variable	July
$\delta(\overline{R}-\overline{E})$	−0.84
Term D $\left(=-\frac{1}{g}\int_{p_{\text{top}}}^{p_{\text{surf}}}\delta\overline{q}\nabla\cdot\overline{\mathbf{V}}_{\text{L20th}}\,dp\right)$	0
Term E $\left(=-\frac{1}{g}\int_{p_{\text{top}}}^{p_{\text{surf}}}\overline{q}_{\text{L20th}}\nabla\cdot\delta\overline{\mathbf{V}}\right)$	−0.94
Term F $\left(=-\frac{1}{g}\int_{p_{\text{top}}}^{p_{\text{surf}}}\overline{\mathbf{V}}_{\text{L20th}}\cdot\nabla\delta\overline{q}\right)$	0.74
Term J $\left(=-\frac{1}{g}\int_{p_{\text{top}}}^{p_{\text{top}}}\delta\overline{\mathbf{V}}\cdot\nabla\overline{q}_{\text{L20th}}\right)$	−0.16
Term K $\left[=-\frac{1}{g}\int_{p_{\text{top}}}^{p_{\text{surf}}}\nabla\cdot\delta(\overline{\mathbf{V}'q'})\,dp\right]$	−0.42
Term G × 100 $\left(=-\frac{1}{g}\int_{p_{\text{top}}}^{p_{\text{surf}}}\delta\overline{qc}\nabla\cdot\overline{\mathbf{V}}_{\text{L20th}}\,dp\times 100\right)$	0.45
Term H × 100 $\left(=-\frac{1}{g}\int_{p_{\text{top}}}^{p_{\text{surf}}}\overline{qc}_{\text{L20th}}\nabla\cdot\delta\overline{\mathbf{V}}\times 100\right)$	−0.34
Term I × 10 $\left(=-\frac{1}{g}\int_{p_{\text{top}}}^{p_{\text{surf}}}\overline{\mathbf{V}}_{\text{L20th}}\cdot\nabla\delta\overline{qc}\times 10\right)$	0.13
Term M × 100 $\left(=\frac{1}{g}\int_{p_{\text{top}}}^{p_{\text{top}}}\delta\overline{\mathbf{V}}\cdot\nabla\overline{qc}_{\text{L20th}}\times 100\right)$	−0.53
Term N × 10 $\left(=-\frac{1}{g}\int_{p_{\text{top}}}^{p_{\text{surf}}}\nabla\cdot\delta(\overline{\mathbf{V}'qc'})\,dp\times 10\right)$	0.35
(Term B + term C + term L + term O + term P) × 10	−0.10

The dynamic change due to advection [term J $=-(1/g)\int_{p_{\text{top}}}^{p_{\text{top}}}\delta\overline{\mathbf{V}}\cdot\nabla\overline{q}_{\text{L20th}}\,dp$ of Eq. (5); Fig. 7e] show a much smoother tendency than terms E (Fig. 7c) and F (Fig. 7d). This term (J) tends to cause a surplus of freshwater flux over West Florida Shelf. Over PF, this term shows a positive and a negative tendency along its western and eastern coasts (Fig. 7e), respectively. But overall, term J causes a negative tendency over PF (Table 3).

The changes in moisture flux convergence from transient eddies [term K $=-(1/g)\int_{p_{\text{top}}}^{p_{\text{surf}}}\nabla\cdot\delta(\overline{\mathbf{V}'q'})\,dp$ of Eq. (5); Fig. 7f] show an overall drying tendency over PF (Table 3). The strong spatial heterogeneity of this term is, however, apparent in Fig. 7f. The remaining forcing terms of $\delta(\overline{R}-\overline{E})$ of Eq. (5) are extremely small (Figs. 7g–l and Table 3).

The term F of Eq. (5) can be further interrogated to ascertain if changes in the horizontal gradients of specific humidity is a result of the changes in temperature of the atmosphere (aka a consequence of the Clausius–Clapeyron equation) or a result of the changes in the circulation. Following Seager et al. (2010), one could calculate changes in term F that would occur if the winds and the relative humidity are kept unchanged. In this case, the specific humidity will change only because of the change in temperature of the atmosphere. Although, one should note that temperature changes can also happen from circulation changes. Nonetheless, this breakdown as Seager et al. (2010) argue is useful as it provides further insight into the direct impact of circulation on humidity and the indirect impact of circulation on humidity via the change in temperature.

The change in specific humidity can be written as

$$\delta\overline{q}=\delta(\overline{r}\overline{q}_s)=\overline{r}_{\text{L20th}}\delta\overline{q}_s+\overline{q}_{s\text{M21st}}\delta\overline{r}, \tag{6}$$

where $\overline{r}$, $\overline{q}_s$, $\overline{r}_{\text{L20th}}$, $\overline{q}_{s\text{M21st}}$ are mean relative humidity, saturation specific humidity, relative humidity from the late twentieth century and saturation-specific humidity from the mid-twenty-first-century simulations of the RCM, respectively. Substituting, Eq. (6) into term F of Eq. (5), we have

$$\text{term F}=-\frac{1}{g}\int_{p_{\text{top}}}^{p_{\text{surf}}}\overline{\mathbf{V}}_{\text{L20th}}\cdot\nabla\delta\overline{q}\,dp=-\frac{1}{g}\int_{p_{\text{top}}}^{p_{\text{surf}}}\overline{\mathbf{V}}_{\text{L20th}}\cdot\nabla(\overline{r}_{\text{L20th}}\delta\overline{q}_s+\overline{q}_{s\text{M21st}}\delta\overline{r})\,dp$$
$$=\overbrace{-\frac{1}{g}\int_{p_{\text{top}}}^{p_{\text{surf}}}\overline{\mathbf{V}}_{\text{L20th}}\cdot\nabla(\overline{r}_{\text{L20th}}\delta\overline{q}_s)\,dp}^{\text{Term A}_1}\overbrace{-\frac{1}{g}\int_{p_{\text{top}}}^{p_{\text{surf}}}\overline{\mathbf{V}}_{\text{L20th}}\cdot\nabla(\overline{q}_{s\text{M21}^{st}}\delta\overline{r})\,dp}^{\text{Term A}_2}. \tag{7}$$

So, terms A_1 and A_2 of Eq. (7) represent the contribution to term F of Eq. (5) from changes in specific humidity between the future and the current climate in the RCM simulation from corresponding changes in saturation specific humidity and relative humidity, respectively. Term A_1 represents changes in humidity in response to Clausius–Clapeyron equation while term A_2 represents changes in humidity affected by circulation changes.

Figure 8 shows this split of the term F as per Eq. (7). It is apparent from this figure that the contributions of terms A_1 (Fig. 8b) and A_2 (Fig. 8c) are insignificant and dominant, respectively. In other words, the Clausius–Clapeyron impact is much smaller than the impact of circulation on projected changes of humidity gradients. This result further illuminates on the fact that the projected hydroclimate changes over PF is nontrivial and does not follow simple heuristic estimation based on Clausius–Clapeyron equation as may be evident in the large scale (Seager et al. 2010).

e. The changes in circulation

In this section we try to understand the associated circulation changes that cause the projected change in the summer hydroclimate over PF in the RCM simulations. In Fig. 9a and b we show the mean July 850-hPa circulation overlaid with the corresponding vertical pressure velocity at 500 hPa and SST from the current and the future RCM simulations. Their corresponding difference is shown in Fig. 9c. The low-level anticyclonic circulation of the North Atlantic subtropical high (NASH) becomes stronger in the future climate (Fig. 9b) relative to the current climate (Fig. 9a). This results in stronger easterlies and stronger southwesterlies, south and north of 26°N in the future warmer climate with overall easterly

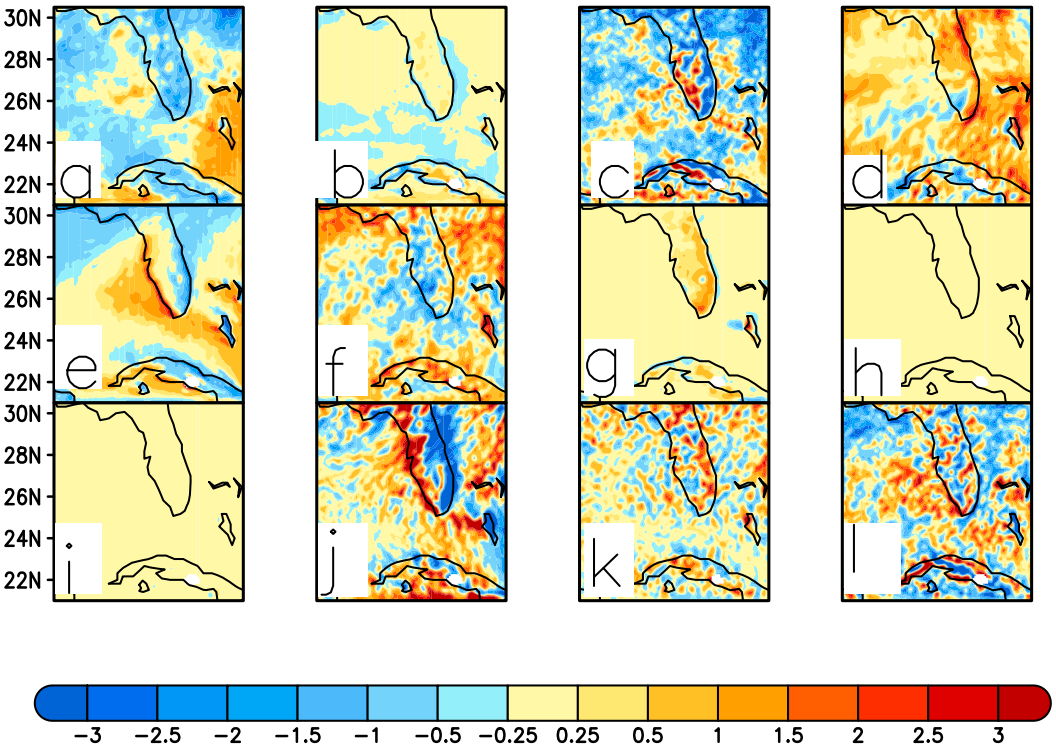

FIG. 7. The change in the moisture budget (mm day^{-1}) between the mid-twenty-first century (2041–60) and the current climate (1986–2005) RCM simulations showing (a) $\delta(\overline{R}-\overline{E})$, (b) term D $[=-(1/g)\int_{p_{\rm top}}^{p_{\rm surf}}\delta\overline{q}\nabla\cdot\overline{\mathbf{V}}_{\rm L20th}\,dp]$, (c) term E $[=-(1/g)\int_{p_{\rm top}}^{p_{\rm surf}}\overline{q}_{\rm L20th}\nabla\cdot\delta\overline{\mathbf{V}}]$, (d) term F $[=-(1/g)\int_{p_{\rm top}}^{p_{\rm surf}}\overline{\mathbf{V}}_{\rm L20th}\cdot\nabla\delta\overline{q}]$, (e) term J $[=-(1/g)\int_{p_{\rm top}}^{p_{\rm top}}\delta\overline{\mathbf{V}}\cdot\nabla\overline{q}_{\rm L20th}]$, (f) term K $[=-(1/g)\int_{p_{\rm top}}^{p_{\rm surf}}\nabla\cdot\delta(\overline{\mathbf{V}'q'})\,dp]$, (g) term G $\times$ 100 $=-(1/g)\int_{p_{\rm top}}^{p_{\rm surf}}\delta\overline{qc}\nabla\cdot\overline{\mathbf{V}}_{\rm L20th}\,dp\times100]$, (h) term H $\times$ 100 $[=-(1/g)\int_{p_{\rm top}}^{p_{\rm surf}}\overline{qc}_{\rm L20th}\nabla\cdot\delta\overline{\mathbf{V}}\times100]$, (i) term I $\times$ 10 $[=-(1/g)\int_{p_{\rm top}}^{p_{\rm surf}}\overline{\mathbf{V}}_{\rm L20th}\cdot\nabla\delta\overline{qc}\times10]$, (j) term M $\times$ 100 $[=-(1/g)\int_{p_{\rm top}}^{p_{\rm top}}\delta\overline{\mathbf{V}}\cdot\nabla\overline{qc}_{\rm L20th}\times100]$, (k) term N $\times$ 10 $[=-1/g\int_{p_{\rm top}}^{p_{\rm surf}}\nabla\cdot\delta(\overline{\mathbf{V}'qc'})\,dp\times10]$, and (l) (term B + term C + term L + term O + term P) $\times$ 10 $\{=[-\partial\delta\overline{W}/\partial t-\partial\delta\overline{C}/\partial t-(1/g)\int_{p_{\rm top}}^{p_{\rm surf}}\nabla\cdot(\delta\overline{\mathbf{V}}\delta\overline{q})\,dp-(1/g)\int_{p_{\rm top}}^{p_{\rm surf}}\nabla\cdot(\delta\overline{\mathbf{V}}\delta\overline{qc})\,dp-\delta R]\times10\}$ computed as a residue of Eq. (5) for July.

anomalies over the domain (Fig. 9c). The mean 500-hPa pressure velocity (used as a proxy for convection) shows upward motion gets stronger over the West Florida Shelf and over the Caribbean region in the domain while it becomes weaker over PF. This is consistent with SSTs becoming warmer, especially over the Caribbean Sea and the West Florida Shelf in the future climate simulation by over 1°C (Fig. 9c). As a result of these changes, the low-level (850 hPa) moisture flux

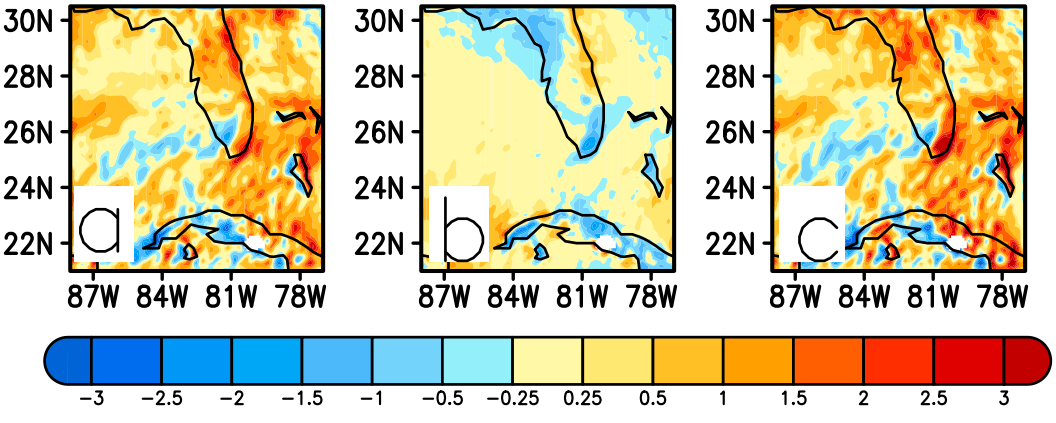

FIG. 8. (a) Term F $=-(1/g)\int_{p_{\rm top}}^{p_{\rm surf}}\overline{\mathbf{V}}_{\rm L20th}\cdot\nabla\delta\overline{q}$, (b) term $A_1=-(1/g)\int_{p_{\rm top}}^{p_{\rm surf}}\overline{\mathbf{V}}_{\rm L20th}\cdot\nabla(r_{\rm L20th}\delta\overline{q}_s)\,dp$, and (c) term $A_2=-(1/g)\int_{p_{\rm top}}^{p_{\rm surf}}\overline{\mathbf{V}}_{\rm L20th}\cdot\nabla(\overline{q}_{s\rm M21st}\delta\overline{r})\,dp$ of Eq. (7) for July (all units are mm day^{-1}).

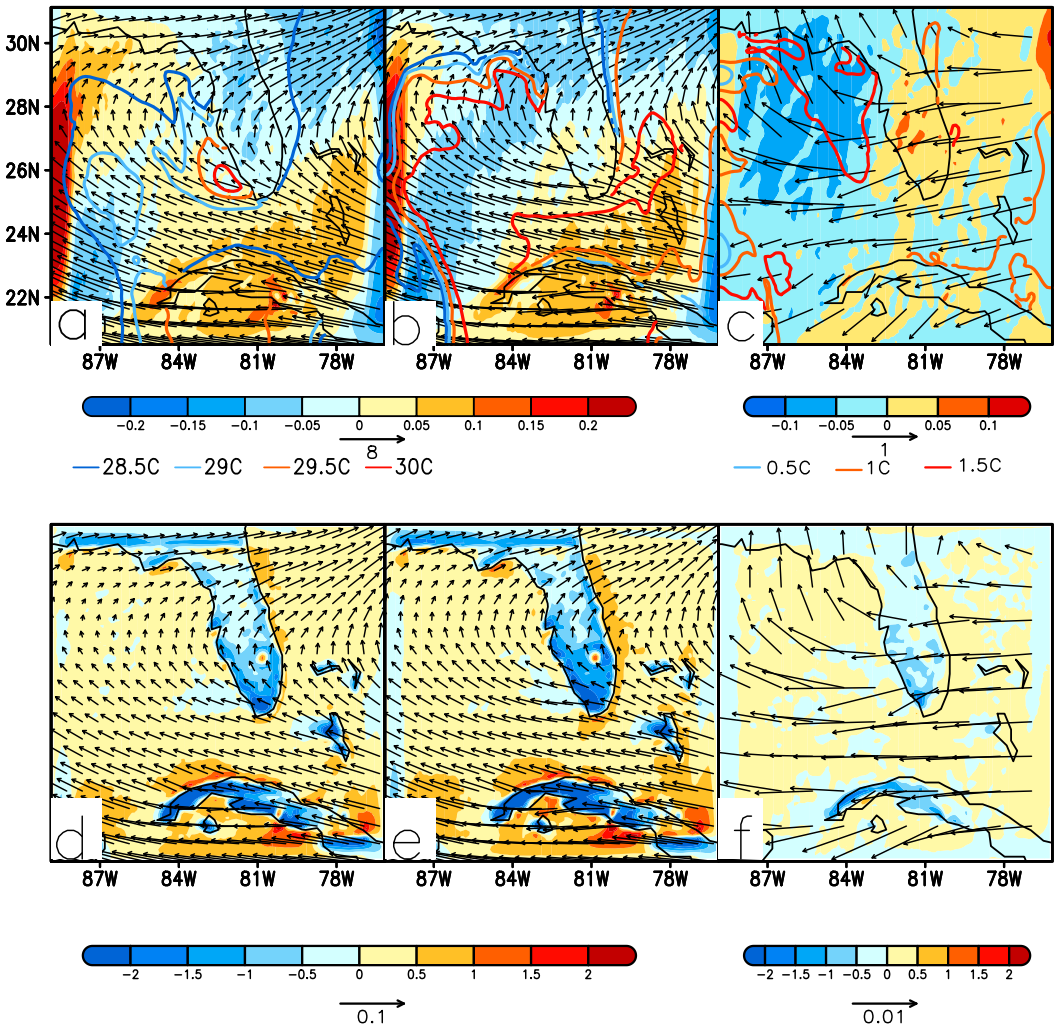

FIG. 9. The mean 850-hPa winds ($m\,s^{-1}$), 500-hPa vertical velocity ($Pa\,s^{-1}$; positive value is upward), and SST (contoured) for July from (a) current climate (1986–2005), (b) future climate (2041–60), and (c) difference of future–current climate simulation of the RCM. Similarly, the moisture flux vectors ($\mathbf{v}q$; $m\,s^{-1}$) and moisture flux convergence ($-\nabla\cdot\overline{\mathbf{v}q}$; positive value is convergence; s^{-1}) at 850 hPa for July from (d) current climate (1986–2005), (e) future climate (2041–60), and (f) difference of future–current climate simulation of the RCM.

convergence and the corresponding moisture flux vectors show an important change in the future compared to the current climate (Figs. 9d–f). In a future warm climate, the RCM simulation suggests that the mean summer moisture flux convergence increases over the West Florida Shelf while it reduces over PF (Fig. 9f). The moisture flux vectors show that the enhanced convection over the West Florida Shelf is dominated by the moisture flow from the Atlantic, which is consistent with the stronger NASH circulation in the future climate (Fig. 9c).

5. Conclusions

In this paper, we have examined in detail the moisture budget from a pair of regional climate model (RCM) integrations centered over Peninsular Florida (PF) and forced with Community Climate System Model version 4 (CCSM4) over a 20-yr period representing the current (1986–2005) and the future (2041–60) climate. These integrations are unprecedented for their spatial resolution as they have been downscaled using a regional coupled ocean–atmosphere model conducted at 10-km grid spacing for both components. Such horizontal resolution is necessary for a region like Florida, where there is considerable coastline, complex ocean bathymetry, and associated ocean circulations which give rise to a very distinct seasonality to the region. Misra et al. (2019) indicated that the projected change in precipitation over PF from the RCM is contrary to CCSM4 with the former projecting a relatively drier climate especially in the summer while the latter projects a wetter summer. An extensive thermodynamic budget conducted in Misra et al. (2019) suggest that the projected future increase in atmospheric shortwave heat flux over the West Florida Shelf, consistent with proportional decrease in low-level clouds in the RCM results in considerable

warming of the shallow West Florida Shelf, which in turn has a bearing on the hydroclimate over PF. The interest in this study, however, is to dwell further into the hydroclimate projections from the RCM over PF and the surrounding oceans from these high-resolution RCM integrations.

The RCM is shown to validate reasonably well with observations of precipitation, surface temperature, and precipitable water. The seasonal cycle of the freshwater flux in the late-twenty-first-century RCM simulation is slightly different from that of precipitation with the former peaking in October while the latter peaks in July. Interestingly, the twentieth-century simulation of RCM shows that none of the forcing terms of Eq. (3) exactly follow the seasonal cycle of the freshwater flux. The dominant terms of the moisture budget of the late-twentieth-century RCM simulation are tendency of moisture due to divergence of moisture, advection of moisture, and moisture flux convergence by transient eddies. The terms involving the cloud water mixing ratio were extremely small.

The projected change (of deficit) in precipitation is, however, statistically significant only in the summer. This results in a projected deficit of the freshwater flux in the mid-twenty-first century relative to the late-twentieth-century RCM simulation. This projected change in freshwater flux is enabled by the dynamic contribution of the change in circulation causing the projected change in the divergence of moisture [term E of Eq. (5)], the thermodynamic contribution of the change in humidity that causes the change in advection of moisture [term F of Eq. (5)], the dynamic contribution of the change in circulation causing the projected change in the advection of moisture [term J of Eq. (5)] and the change in moisture flux convergence from transient eddies [term K of Eq. (5)]. The contribution of term F of Eq. (5) was further interrogated, which revealed that humidity changes due to temperature changes (aka the Clausius–Clapeyron effect) are less important than humidity changes due to relative humidity changes (aka a result of circulation changes).

Further analysis of these changes reveals that the low-level, mean summer anticyclonic circulation of the North Atlantic subtropical high becomes stronger with a corresponding increase in SST over the Caribbean Sea and the West Florida Shelf in the future RCM simulation. As a consequence of these circulation changes, the mean summer moisture flux convergence increases over the West Florida Shelf while a reduction occurs over PF resulting in the reduction of precipitation over PF at the expense of the increase in precipitation over the West Florida Shelf.

The obvious limitation of this study is that we are examining the moisture budget changes from only one RCM with one emission scenario of RCP8.5, which does not account for the uncertainty in model projections, other emission scenarios, and internal variability. This is largely because the computational resources in running the RCM at 10-km grid spacing for both the atmospheric and the oceanic components is expensive, which makes downscaling multiple global models an onerous task. But our earlier studies have clearly established that this type of numerical tool (RCM) is important for this region to resolve the complex ocean bathymetries that is critical for the upper-ocean circulation and to depict the ocean–land contrast realistically. Therefore, we believe that understanding the projected change in the hydroclimate from this single RCM simulation is an important step to motivate further broadening of this type of investigation with a more robust estimate of the associated uncertainties.

Acknowledgments. This work was supported by grants from NASA Grants 80NSSC19K1199 and NNX17AG72G and the South Florida Water Management District (PO 039231). The supercomputing facility provided by XSEDE under Grant ATM10010 was used in addition to the Florida State University High Performance Computing Cluster to complete the model integrations used in this study. CPC Global Temperature data are provided by the NOAA/OAR/ESRL PSL, Boulder, Colorado, from their website at https://psl.noaa.gov/.

Data availability statement. The validation datasets are available from public repositories cited in the text and in the acknowledgments. The authors were unable to find a valid data repository for the model data used in this study. These data are available from the first author (vmisra@fsu.edu) upon request.

REFERENCES

Alpert, J. C., M. Kanamitsu, P. M. Caplan, J. G. Sela, G. White, and E. Kalnay, 1988: Mountain induced gravity wave drag parameterization in the NMC medium-range forecast model. *Proc. Eighth Conf. on Numerical Weather Prediction*, Baltimore, MD, Amer. Meteor. Soc., 726–733.

Bastola, S., and V. Misra, 2013: Sensitivity of hydrological simulations of southeastern United States watersheds to temporal aggregation of rainfalls. *J. Hydrometeor.*, **14**, 1334–1344, https://doi.org/10.1175/JHM-D-12-096.1.

Bhardwaj, A., and V. Misra, 2019: The role of air-sea coupling in the downscaled hydroclimate projection over Peninsular Florida and the West Florida Shelf. *Climate Dyn.*, **53**, 2931–2947, https://doi.org/10.1007/s00382-019-04669-5.

Chou, M.-D., and M. J. Suarez, 1994: An efficient thermal infrared radiation parameterization for use in general circulation models. NASA Tech. Memo. 104606, Vol. 3, 85 pp., https://ntrs.nasa.gov/search.jsp?R=19950009331.

——, and K-T. Lee, 1996: Parameterizations for the absorption of solar radiation by water vapor and ozone. *J. Atmos. Sci.*, **53**, 1203–1208, https://doi.org/10.1175/1520-0469(1996)053<1203:PFTAOS>2.0.CO;2.

Ek, M. B., K. E. Mitchell, Y. Lin, E. Rogers, P. Grunmann, V. Koren, G. Gayno, and J. D. Tarpley, 2003: Implementation of Noah land surface model advances in the National Centers for Environmental Prediction operational mesoscale Eta model. *J. Geophys. Res.*, **108**, 8851, https://doi.org/10.1029/2002JD003296.

Gent, P. R., and Coauthors, 2011: The Community Climate System Model version 4. *J. Climate*, **24**, 4973–4991, https://doi.org/10.1175/2011JCLI4083.1.

Haidvogel, D. B., H. G. Arango, K. Hedstrom, A. Beckmann, P. Malanotte-Rizzoli, and A. F. Shchepetkin, 2000: Model evaluation experiments in the North Atlantic basin: Simulations in nonlinear terrain-following coordinates. *Dyn. Atmos. Oceans*, **32**, 239–281, https://doi.org/10.1016/S0377-0265(00)00049-X.

Ham, S., K. Yoshimura, and H. Li, 2016: Historical dynamical downscaling for East Asia with the Atmosphere and Ocean Coupled Regional Model. *J. Meteor. Soc. Japan*, **94A**, 199–208, https://doi.org/10.2151/jmsj.2015-046.

Held, I. M., and B. J. Soden, 2006: Robust responses of the hydrological cycle to global warming. *J. Climate*, **19**, 5686–5699, https://doi.org/10.1175/JCLI3990.1.

Hong, S. Y., and H. L. Pan, 1996: Nonlocal boundary layer vertical diffusion in a medium-range forecast model. *Mon. Wea. Rev.*, **124**, 2322–2339, https://doi.org/10.1175/1520-0493(1996)124<2322:NBLVDI>2.0.CO;2.

Huffman, G. J., D. T. Bolvin, E. J. Nelkin, and J. Tan, 2019: Integrated Multi-satellitE Retreivals for GPM (IMERG) technical documentation. NASA Tech. Doc., 77 pp., https://gpm.nasa.gov/sites/default/files/document_files/IMERG_doc_190909.pdf.

Juang, H. M., and M. Kanamitsu, 1994: The NMC nested regional spectral model. *Mon. Wea. Rev.*, **122**, 3–26, https://doi.org/10.1175/1520-0493(1994)122<0003:TNNRSM>2.0.CO;2.

Kirtman, B. P., and Coauthors, 2012: Impact of ocean model resolution on CCSM climate simulations. *Climate Dyn.*, **39**, 1303–1328, https://doi.org/10.1007/s00382-012-1500-3.

——, V. Misra, R. Burgman, J. Infanti, and J. Obeysekera, 2017: Florida climate variability and prediction. *Florida's Climate: Changes, Variations, and Impacts*, E. P. Chassignet et al., Eds., Florida Climate Institute, 511–532, https://doi.org/10.17125/fci2017.ch17.

Kunkel, K. E., T. R. Karl, M. F. Squires, X. Yin, T. S. Stegall, and D. Easterling, 2013: Precipitation extremes: Trends and relationships with average precipitation and precipitable water in the contiguous United States. *J. Appl. Meteor. Climatol.*, **59**, 125–142, https://doi.org/10.1175/JAMC-D-19-0185.1.

Large, W. G., J. C. McWilliams, and S. C. Doney, 1994: Oceanic vertical mixing: A review and a model with a nonlocal boundary layer parameterization. *Rev. Geophys.*, **32**, 363–403, https://doi.org/10.1029/94RG01872.

Li, H., M. Kanamitsu, and S. Y. Hong, 2012: California reanalysis downscaling at 10 km using an ocean-atmosphere coupled regional model system. *J. Geophys. Res.*, **117**, D12118, https://doi.org/10.1029/2011JD017372.

——, ——, ——, K. Yoshimura, D. R. Cayan, and V. Misra, 2014: A high-resolution ocean-atmosphere coupled downscaling of the present climate over California. *Climate Dyn.*, **42**, 701–714, https://doi.org/10.1007/s00382-013-1670-7.

Liu, Y., S. K. Lee, D. B. Enfield, B. A. Muhling, J. T. Lamkin, F. E. Muller-Karger, and M. A. Roffer, 2015: Potential impact of climate change on the Intra-Americas Sea: Part-1. A dynamic downscaling of the CMIP5 model projections. *J. Mar. Syst.*, **148**, 56–69, https://doi.org/10.1016/j.jmarsys.2015.01.007.

Mellor, G. L., and T. Yamada, 1982: Development of a turbulence closure model for geophysical fluid problems. *Rev. Geophys.*, **20**, 851–875, https://doi.org/10.1029/RG020i004p00851.

Misra, V., and A. Mishra, 2016: The oceanic influence on the rainy season of Peninsular Florida. *J. Geophys. Res. Atmos.*, **121**, 7691–7709, https://doi.org/10.1002/2016JD024824.

——, ——, and A. Bhardwaj, 2017a: High-resolution regional-coupled ocean–atmosphere simulation of the Indian Summer Monsoon. *Int. J. Climatol.*, **37**, 717–740, https://doi.org/10.1002/joc.5034.

——, C. Selman, A. J. Waite, S. Bastola, and A. Mishra, 2017b: Terrestrial and ocean climate of the 20th century. *Florida's Climate: Changes, Variations, and Impacts*, E. P. Chassignet et al., Eds., Florida Climate Institute, 485–509, https:/doi.org/10.17125/fci2017.ch17.

——, A. Mishra, and A. Bhardwaj, 2018: Simulation of the intra-seasonal variations of the Indian summer monsoon in a regional coupled ocean–atmosphere model. *J. Climate*, **31**, 3167–3185, https://doi.org/10.1175/JCLI-D-17-0434.1.

——, ——, and ——, 2019: A coupled ocean-atmosphere downscaled climate projection for the peninsular Florida region. *J. Mar. Syst.*, **194**, 25–40, https://doi.org/10.1016/j.jmarsys.2019.02.010.

Moorthi, S., and M. J. Suarez, 1992: Relaxed Arakawa–Schubert: A parameterization of moist convection for general circulation models. *Mon. Wea. Rev.*, **120**, 978–1002, https://doi.org/10.1175/1520-0493(1992)120<0978:RASAPO>2.0.CO;2.

Putrasahan, D. A., I. Kamenkovich, L. M. Henaff, and B. P. Kirtman, 2017: Importance of ocean mesoscale variability for air-sea interactions in the Gulf of Mexico. *Geophys. Res. Lett.*, **44**, 6352–6362, https://doi.org/10.1002/2017GL072884.

Seager, R., N. Naik, and G. A. Vecchi, 2010: Thermodynamic and dynamic mechanisms for large-scale changes in the hydrological cycle in response to global warming. *J. Climate*, **23**, 4651–4668, https://doi.org/10.1175/2010JCLI3655.1.

Selman, C., V. Misra, L. Stefanova, S. DiNapoli, and T. J. Smith III, 2013: On the twenty first century wet season projections over the Southeastern United States. *Reg. Env. Changes*, **13**, 153–164, https://doi.org/10.1007/S10113-013-0477-8.

Shchepetkin, A. F., and J. C. McWilliams, 2005: The Regional Oceanic Modeling System (ROMS): A split-explicit, free-surface, topography-following-coordinate oceanic model. *Ocean Modell.*, **9**, 347–404, https://doi.org/10.1016/j.ocemod.2004.08.002.

Taylor, K. E., R. J. Stouffer, and G. A. Meehl, 2012: An overview of CMIP5 and the experiment design. *Bull. Amer. Soc*, **93**, 486–498, https://doi.org/10.1175/BAMS-D-11-00094.1.

Tiedtke, M., 1983: The sensitivity of the time-mean large-scale flow to cumulus convection in the ECMWF model. *Proc. of ECMWF Workshop on Convective in Large-scale Models*, Reading, UK, European Centre for Medium-Range Weather Forecasts, 297–316, https://www.ecmwf.int/node/12733.

Trenberth, K., and C. J. Guillemot, 1995: Evaluation of the global atmospheric moisture budget as seen from analyses. *J. Climate*, **8**, 2255–2272, https://doi.org/10.1175/1520-0442(1995)008<2255:EOTGAM>2.0.CO;2.

Trenberth, K. E., A. Dai, R. M. Rasmussen, and D. B. Parsons, 2003: The changing character of precipitation. *Bull. Amer. Meteor. Soc.*, **84**, 1205–1218, https://doi.org/10.1175/BAMS-84-9-1205.

Umlauf, L., and H. Burchard, 2003: A generic length-scale equation for geophysical turbulence models. *J. Mar. Res.*, **61**, 235–265, https://doi.org/10.1357/002224003322005087.

USGCRP, 2018: *Impacts, Risks, and Adaptation in the United States*. Vol. II, *Fourth National Climate Assessment*, D. R. Reidmiller et al., Eds., U.S. Global Change Research Program, 1515 pp., https://doi.org/10.7930/NCA4.2018.

Utsumi, N., S. Seto, S. Kanae, E. E. Maeda, and T. Oki, 2011: Does higher surface temperature intensify extreme precipitation? *Geophys. Res. Lett.*, **38**, L16708, https://doi.org/10.1029/2011GL048426.

Westra, S., and Coauthors, 2014: Future changes to the intensity and frequency of short duration extreme rainfall. *Rev. Geophys.*, **52**, 522–555, https://doi.org/10.1002/2014RG000464.

Zhao, Q., and F. H. Carr, 1997: A prognostic cloud scheme for operational NWP models. *Mon. Wea. Rev.*, **125**, 1931–1953, https://doi.org/10.1175/1520-0493(1997)125<1931:APCSFO>2.0.CO;2.